



1 Observation System Simulation Experiments in the Atlantic 2 Ocean for enhanced surface ocean $p\text{CO}_2$ reconstructions.

3 Anna Denvil-Sommer^{1,2}, Marion Gehlen², Mathieu Vrac²

4
5 ¹School of Environmental Sciences, University of East Anglia, Norwich, UK

6 ²Laboratoire des Sciences du Climat et de l'Environnement (LSCE), Institut Pierre Simon Laplace (IPSL),
7 CNRS/CEA/UVSQ/Univ. Paris-Saclay, Orme des Merisiers, Gif Sur Yvette, 91191, France

8 *Correspondence to:* Anna Denvil-Sommer (anna.sommer.lab@gmail.com)

9

10

11 **Abstract.** To derive an optimal observation system for surface ocean $p\text{CO}_2$ in the Atlantic Ocean and the Atlantic
12 sector of the Southern Ocean eleven Observation System Simulation Experiments (OSSEs) were completed. Each
13 OSSE is a Feed-Forward Neural Network (FFNN) that is based on a different data distribution and provides ocean
14 surface $p\text{CO}_2$ for the period 2008-2010 with a 5 day time interval. Based on the geographical and time positions
15 from three observational platforms, volunteering observing ships (VOS), Argo floats and OceanSITES moorings,
16 pseudo-observations were constructed using the outputs from an online-coupled physical-biogeochemical global
17 ocean model with 0.25° nominal resolution. The aim of this work was to find an optimal spatial distribution of
18 observations to supplement the widely used Surface Ocean CO_2 Atlas (SOCAT) and to improve the accuracy of
19 ocean surface $p\text{CO}_2$ reconstructions. OSSEs showed that the additional data from mooring stations and an
20 improved coverage of the Southern Hemisphere with biogeochemical ARGO floats corresponding to least 25% of
21 the density of active floats (2008-2010) (OSSE 10) would significantly improve the $p\text{CO}_2$ reconstruction and
22 reduce the bias of derived estimates of sea-air CO_2 fluxes by 74% compared to ocean model outputs.
23

24 1 Introduction

25

26 The ocean is a major sink of anthropogenic CO_2 (Ciais et al., 2013; Friedlingstein et al., 2020). For the period
27 2010-2019 the ocean uptake was 2.5 ± 0.6 GtC/yr with a strong intensification (from 1.9 to 3.1 GtC/yr) along with
28 the increase of CO_2 emissions (Friedlingstein et al., 2020). The ocean carbon sink estimate is derived from Global
29 Ocean Biogeochemical Models (Hauck et al., 2020) and data-based reconstructions of surface ocean partial
30 pressures of carbon dioxide ($p\text{CO}_2$). The data-based reconstructions rely on the interpolation of surface ocean
31 $p\text{CO}_2$ - derived from measurements of surface ocean CO_2 fugacity - by a variety of methods (e.g. Watson et al.,
32 2020; Gregor et al., 2019; Denvil-Sommer et al., 2019; Bittig et al., 2018; Landschützer et al., 2013, 2016;
33 Rödenbeck et al., 2014, 2015; Fay et al., 2014; Zeng et al., 2014; Nakaoka et al., 2013; Schuster et al., 2013;
34 Takahashi et al., 2002, 2009). These methods provide converging estimates of the global ocean carbon sink and
35 its variability at seasonal and interannual time scales (Rödenbeck et al., 2015; Denvil-Sommer et al., 2019). They
36 are, however, sensitive to the observation coverage in space and time which contributes to inconsistent results over
37 regions with sparse data (Denvil-Sommer et al., 2019; Rödenbeck et al., 2015) and to persistent uncertainties at
38 global scale (Gregor et al., 2019; Hauck et al., 2020).
39

40 The majority of observations contributing to the Surface Ocean CO_2 Atlas (SOCAT) (Bakker et al., 2016) are still
41 obtained by underway sampling systems on board of volunteering observing ships. The data density is not
42 homogenous, with Southern latitudes being less well sampled in space and also in time. Sparse data coverage and
43 the lack of observations covering the full seasonal cycle challenge mapping methods and result in noisy
44 reconstructions of surface ocean $p\text{CO}_2$ and disagreements between different models (Denvil-Sommer et al., 2019,
45 Rödenbeck et al., 2015). The ship-based sampling effort is progressively complemented by autonomous observing
46 platforms, such as biogeochemical ARGO floats equipped with pH sensors. The expansion of the observing system
47 to autonomous platforms is of particular relevance in regions that are undersampled either because of the presence
48 of fewer regular shipping lines (e.g., South Atlantic) or because adverse weather conditions prevent a year around
49 sampling (e.g., Southern Ocean). The benefits of combining ship-based measurements of $p\text{CO}_2$ and data from



50 biogeochemical ARGO floats was recently demonstrated for the assessment of Southern Ocean CO₂ fluxes
51 (Bushinsky et al., 2019).
52

53 This study extended the scope to the Atlantic basin, including the Atlantic sector of the Southern Ocean. It explored
54 design options for a future augmented Atlantic scale observing system which would optimally combine data
55 streams from various platforms and contribute to reduce the bias in reconstructed surface ocean *p*CO₂ fields and
56 sea-air CO₂ fluxes. A series of Observation System Simulation Experiments (OSSEs) were carried out in a perfect
57 model framework using output from an online-coupled physical-biogeochemical global ocean model at 1/4°
58 nominal resolution. Since all fields used by the FFNN are produced by the same model run and thus internally
59 consistent, the comparison between reconstructed and modelled *p*CO₂ distributions allows to assess the theoretical
60 skill for each experiment. Starting from measurements extracted from the SOCAT database, the goal was to
61 identify how and where the new data from biogeochemical ARGO floats can improve surface ocean *p*CO₂
62 reconstructions and how to optimally integrate them with other existing platforms. *Pseudo-observations* were
63 obtained by sub-sampling model output at sites of real-world observations. Surface ocean *p*CO₂ was reconstructed
64 from these pseudo-observations at basin scale by applying a non-linear feed forward neural network (FFNN)
65 (Bishop, 1995; Rumelhart et al., 1986). The choice of the FFNN for our experiments was motivated by its overall
66 performance reported in Denvil-Sommer et al. (2019). The architecture of the FFNN method was adapted to the
67 current problem and differs from the one presented in Denvil-Sommer et al. (2019).
68

69 The remainder of the article is structured into Section 2 presenting the model output, the observing systems and
70 observations as well as the design experiments, and the description of the statistical model. Results are presented
71 and discussed in Section 3. Section 4 is dedicated to the conclusion and the presentation of perspectives.
72

73 2 Data and methods

74
75 Here we present the ensemble of observing systems that either already perform measurements to estimate *p*CO₂
76 or have the possibility to be equipped with new sensors to provide biogeochemical measurements (Williams et al.,
77 2017). These datasets provide information on geographical, as well as time positions and hence on the distribution
78 of *p*CO₂ measurements. In this section we also describe the ocean model output and how we use it in the OSSEs.
79 As mentioned in the introduction the data from the model co-localized with real positions of observing-systems
80 are called *pseudo-observations*.
81

82 2.1 Data

84 a) Observing systems

85 Three observing systems were selected for the study: (1) volunteering observing ships providing *in situ*
86 measurements of surface ocean CO₂ fugacity (*f*CO₂), (2) moorings (OceanSITES), and (3) profilers (Argo). These
87 observations form the dataset of geographical and time positions for our experiments. Surface ocean measurements
88 of *f*CO₂ from multiple platforms are converted to *p*CO₂ and compiled in the SOCAT database (Bakker et al., 2016).
89 Moorings are not routinely equipped with sensors of CO₂ fugacity, though, we used their geographical positions
90 to identify possible locations for additional measurements. Biogeochemical ARGO floats are increasingly
91 equipped with pH sensors allowing computing *p*CO₂ from pH and SST- based alkalinity. For the design
92 experiments, we considered distributions of physical ARGO floats (2008-2011) from Gasparin et al. (2019) and
93 supposed that they were equipped with *p*CO₂ sensors.
94

95 (1) **SOCAT database v5** (Bakker et al., 2016; (<https://www.socat.info/index.php/data-access/>)): the database
96 provides a good coverage of the Northern Hemisphere. Data for the period 2001-2010 were used, representing
97 ~60% of data in SOCAT database (Fig. 1a). We used the **synthesis files SOCATv5** with the daily measurements.
98 There are 24 moorings in SOCATv5 that provided CO₂ fugacity measurements between 2001 and 2010. These
99 moorings were excluded from OceanSITES data (see below).

100 (2) **Argo profilers**: We used the network of Argo (Gould et al., 2004) distributions provided by Mercator Ocean
101 (details can be found in Gasparin et al., 2019) for the period 2008-2010. It provides a synthetic homogeneous
102 distribution of **1 profiler per 3°x3° grid box**, amounting to 310-360 measurements per day (Fig. 1b) based on real
103 trajectories of Argo floats. This synthetic Argo distribution was built based on the time, date and location of Argo
104 profiles during the 2009–2011 period (Gasparin et al., 2019). To provide a homogeneous coverage Gasparin et al.
105 (2019) removed some float trajectories in well-sampled regions, for example the Gulf Stream, or added floats in



106 the low-sampled Tropical and South Atlantic regions. The target for BioGeoChemical Argo (1/4 of ARGO
107 coverage) (Bittig et al., 2018) was derived from this distribution.
108 (3) **OceanSITES**: This dataset combines observations from open ocean Eulerian time series stations providing
109 data since 1999 (Fig.1c). We used all available locations of moorings (except moorings included in SOCATv5)
110 and added this information to the period of reconstruction 2008-2010 (<http://www.oceansites.org/>). It provided
111 318 additional positions to our data set.

112
113 For this study, the same set of predictors was used as in Denvil-Sommer et al. (2019) for training the Machine
114 Learning (ML) algorithm: sea surface salinity (SSS), sea surface temperature (SST), sea surface height (SSH),
115 mixed layer depth (MLD), chlorophyll *a* concentration (Chl *a*) and atmospheric CO₂ ($pCO_{2,atm}$). These variables
116 are known to represent the main physical, chemical and biological drivers of surface ocean pCO_2 (Takahashi et
117 al., 2009; Landschützer et al., 2013).

118 b) Model output and pseudo-observations

119 Here we used the numerical output from an online-coupled physical-biogeochemical global ocean model, the
120 NEMO/PISCES model, at 5-day resolution. This configuration of the Nucleus for European Modelling of the
121 Ocean (NEMO) framework was implemented on a global tripolar grid. It coupled the ocean general circulation
122 model OPA9 (Madec et al., 1998), the sea ice code LIM2 (Fichefet & Maqueda, 1997), and the biogeochemical
123 model PISCESv1 (Aumont and Bopp, 2006). Information on the simulation is given in Gehlen et al. (2020) and
124 Terhaar et al. (2019). The geographical and time positions identified from the data mentioned before were used to
125 create pseudo-observations by sub-sampling NEMO/PISCES model output at sites of real-world observations.
126 Thus, the positions of SOCAT, Argo floats and mooring stations were chosen over 5 days centred on the
127 NEMO/PISCES date and sub-sampled on the model grid. The model grid coordinate closest to the real
128 geographical position was chosen, if several measurements were co-localized at the same grid coordinate and same
129 time step it is counted as one measurement. No Argo floats were added to grid cells if there was already a
130 measurement identified in the SOCAT database. All predictors and target pCO_2 were taken from model output at
131 corresponding coordinates. These outputs served as the reference for validation and evaluation of our experiments
132 and for assessing the ML method's accuracy. The simulation covers the period 1958 to 2010, the last 3 years were
133 retained for the design study.

134 2.2 Observational System Simulation Experiences

135 Table 1 summarizes experiments designed for different combinations of observing platforms.
136 The first test is based on individual sampling data extracted from the SOCAT database. As mentioned before these
137 data provide a good coverage of the Northern Hemisphere. The lesser coverage in the Southern Hemisphere results
138 in a larger dispersion of methods based on these observations only (Denvil-Sommer et al., 2019; Rödenbeck et al.,
139 2015). This has motivated experiments with additional data from Argo profilers limited to the Southern
140 Hemisphere. An experiment based on the full physical ARGO network was included to evaluate the method for a
141 high spatial and temporal coverage (an optimal, yet unrealistic case).
142

143 We have tested combinations of SOCAT data and (1) total Argo data, (2) Argo only in the Southern Hemisphere,
144 and (3) 25% or (4) 10% of the initial (total) Argo distribution. Finally, these experiments were repeated with
145 additional mooring data. It is worth noting (Table 1) that OSSE 4 is closest to the target of the BGC-Argo program
146 with a BGC-Argo density corresponding to 25% of the existing Argo distribution. However, we decided to choose
147 OSSE 3 as a benchmark against which to evaluate individual experiments. This experiment has a high data density
148 and provides additional information on a potential future BGC-Argo network.

149 2.3 Method

150 We used a Feed-Forward Neural Network (FFNN) based on Denvil-Sommer et al. (2019) to reconstruct surface
151 ocean pCO_2 over the Atlantic Ocean. Compared to the previous study we skipped the first step consisting of the
152 reconstruction of the pCO_2 climatology. The reconstruction covered January 2008 to December 2010 with a 5-day
153 frequency and the spatial resolution of the tripolar ORCA025 model grid (nominal 1/4° resolution). The approach
154 consisted in a method that reconstructs the non-linear relationships between the target pCO_2 and predictors
155 responsible for pCO_2 variability:

$$156 \quad pCO_{2,n} =$$
$$157 \quad f(SSS_n, SST_n, SSH_n, Chl_n, MLD_n, pCO_{2,atm,n}) \quad (1)$$
$$158 \quad SSS_{anom,n}, SST_{anom,n}, SSH_{anom,n}, Chl_{anom,n}, MLD_{anom,n}, pCO_{2,atm,anom,n} lat_n, long_{1,n}, long_{2,n}$$

159



160 As previously (Denvil-Sommer et al., 2019), we use Keras, a high-level neural network Python library (“Keras:
161 the Python Deep Learning library”, Chollet, 2015; <https://keras.io>) to construct and train the FFNN models. We
162 first identified an optimal configuration (number and size of hidden layers, the activation functions etc.) of the
163 FFNN model. Based on our earlier work (Denvil-Sommer et al., 2019), a hyperbolic tangent was chosen as an
164 activation function for neurons in hidden layers, and a linear function was chosen for the output layer. As an
165 optimization algorithm, the mini-batch gradient descent or “RMSprop” was used (adaptive learning rates for each
166 weight, Chollet, 2015; Hinton et al., 2012).

167 The numbers of hidden layers and parameters depend on the number of data used for training. In this work, the
168 FFNN was applied separately for each month (one model for January, one model for February, etc.). A sub-set of
169 50% of data were used for training. 25% participated in the evaluation of the model during the training algorithm,
170 and 25% were used to validate the model after training. These data were chosen regularly in time and space. Tables
171 S1 presents the numbers of training data for each month and each OSSE. To adjust the number of FFNN parameters
172 we followed the empirical rule that suggests using a factor 10 between the number of data and the number of
173 parameters to avoid overfitting (Amari et al., 1997). The FFNNs for all OSSEs except OSSE 2 have four layers
174 (two hidden layers) with 1116 parameters in total. The OSSE 2 which is based on Argo data for the period 2008-
175 2010, has significantly less data for training and thus, the FFNN for the OSSE 2 is different: 3 layers (one hidden
176 layer) with 541 total parameters.

177 It is worth noting that all data have to be normalized before their use in the FFNN as exemplified for SSS:

$$178 \quad SSS_n = \frac{SSS - \overline{SSS}}{STD(SSS)} \quad (2)$$

179 \overline{SSS} is the total mean of variable SSS, $STD(SSS)$ is standard deviation of SSS.

180 Normalization is required to rank all predictors in the same scale, and it allows to avoid the possible influence of
181 one predictor with strong variability (Kallache et al., 2011).

182 Following Denvil-Sommer et al. (2019) we normalized the geographical positions (lat, long) in the following way:

$$183 \quad \begin{aligned} lat_n &= \sin(lat * \pi/180) \\ long_{n,1} &= \sin(long * \pi/180) \end{aligned}$$

$$185 \quad long_{n,2} = \cos(long * \pi/180).$$

186 A K-fold cross-validation was used to evaluate and validate the FFNN architecture. The cross-validation is based
187 on K=4 different subsamples where 25 % of independent data are chosen for validation. In each of the 4 cases the
188 25% of data are different and there is no overlap. Thereby, each run has 4 outputs. The different architectures of
189 the FFNN were tested and the final one was chosen based on skill assessed by the root-mean-square difference
190 (RMSD), the r^2 and the bias of 4 outputs for each architecture. To ensure a good accuracy of the method and check
191 that there is no overfitting, we compared the RMSD, r^2 and bias estimated from the validation dataset with those
192 estimated from the training dataset. Denvil-Sommer et al. (2019) provide a detailed description of the model
193 including the accuracy of the ML method and its ability to correctly reproduce the pCO_2 variability.

194 2.4 Diagnostics

195 The comparison between OSSEs is done per biome, following Rödenbeck et al. (2015) (Fig. 2, Table 2). Biome
196 8, North Atlantic Ice, has been omitted due to poor data coverage in all OSSEs. It is expected that reconstructions
197 over this region will yield large biases susceptible to interfere with the interpretation of results from individual
198 OSSEs.

199 In order to simplify the comparison, we used Taylor and Target Diagrams with standard deviation, biases,
200 correlation and normalized RMSD (uRMSD) of the mean of 4 FFNN outputs for each OSSE. Here uRMSD is
201 estimated as:

$$203 \quad uRMSD = \sqrt{mean(\{ [pCO_{2\ OSSE} - \overline{pCO_{2\ OSSE}}] - [pCO_{2\ NEMO} - \overline{pCO_{2\ NEMO}}] \}^2)} \quad (3)$$

204 For each OSSE and each output of the k-fold cross-validation, we estimated a time mean difference between its
205 pCO_2 and NEMO pCO_2 at each grid point:

$$206 \quad Diff_{j,i} = \text{mean}_T(pCO_{2\ OSSE\ j,i} - pCO_{2\ NEMO}) = \frac{1}{T} \sum_{t=1}^T (pCO_{2\ OSSE\ j,i,t} - pCO_{2\ NEMO,t}),$$



207 where mean_T is a time mean over the period, T is a number of time steps, j is an index of the OSSE and i is an
208 index of output, from 1 to 4.

209 Further, the maximum absolute value from 4 outputs maxValue_j was estimated for each OSSE:

$$210 \quad \text{maxValue}_j = \max_i(\text{abs}(\text{Diff}_{j,i})),$$

211 where \max_i is a maximum value on i , the index of output, for each fixed j , the OSSE index. The index i of the
212 maximum absolute value of FFNN outputs is called i_{max} .

213 The final mean difference meanD_j was estimated as:

$$214 \quad \text{meanD}_j = \text{sign}(\text{Diff}_{j,i_{\text{max}}}) * \text{maxValue}_j, \quad (4)$$

215 where $\text{sign}(x)$ is a function that returns the sign of a value x , -1 or 1.

216 The STD of the mean difference $\text{Diff}_{j,i}$ is estimated for each OSSE as:

$$217 \quad \text{STD}_j = \text{std}(\text{Diff}_{j,i}), \quad (5)$$

218 where j is fixed, and all outputs of FFNN i are included in the estimation of STD.

219
220 The time series of the mean value from 4 FFNN outputs for $p\text{CO}_2$ were provided per biome, with the maximum
221 and minimum values from these 4 outputs in the form of shadow cloud. Also, the time series of CO_2 sea-air flux
222 are shown in the same way as the ones for $p\text{CO}_2$. The sea-air CO_2 flux, $fg\text{CO}_2$, was calculated after Rödenbeck et
223 al. (2015):

$$224 \quad fg\text{CO}_2 = k\rho L(p\text{CO}_2 - p\text{CO}_{2,atm}), \quad (6)$$

225 ρ is seawater density and L is the temperature-dependent solubility (Weiss, 1974). k is the piston velocity estimated
226 as (Wanninkhof, 1992):

$$227 \quad k = \Gamma u^2 (Sc^{CO_2} / Sc^{ref})^{-0.5}.$$

228 The global scaling factor Γ was chosen as in Rödenbeck et al. (2014) with the global mean CO_2 piston velocity
229 equaling 16.5 cm h^{-1} . Sc corresponds to the Schmidt number estimated according to Wanninkhof (1992). The
230 wind speed was computed from 6-hourly NCEP wind speed data (Kalnay et al., 1996). To simplify the
231 interpretation of results the NEMO/PISCES CO_2 air-sea flux was also calculated by using formula (6) and NCEP
232 wind speed.

233 3 Results

234 Figure 3 shows the Taylor Diagram (correlation coefficient between reconstructed $p\text{CO}_2$ and model output, and
235 Standard Deviation of reconstructed fields) of 11 OSSEs in the region of 8 biomes (pink) and in each of these
236 biomes separately (color code corresponds to Fig. 2). The target diagrams per biomes for each OSSE are presented
237 on Figure 4. Over regions well-covered with observations (biomes 9, 10, 11) results of different OSSEs lie close
238 to each other. The OSSE 1 (+; Fig. 3a) that is based only on SOCAT data has a lower correlation coefficient over
239 the whole region (0.67, pink) and per biomes (Fig. 3a). Over regions with poor observational coverage the results
240 from OSSE 1 lie at a distance from others. OSSE 1 also shows the largest normalized RMS differences (uRMSD)
241 (Fig. 4), as exemplified for biome 17 with uRMSD of $17.33 \mu\text{atm}$, STD of $21.11 \mu\text{atm}$ (compared to $24.03 \mu\text{atm}$
242 estimated from NEMO/PISCES data) and bias of $-11.63 \mu\text{atm}$ (all values in the Fig. 3 and 4 are presented in Tables
243 3 and 4). The OSSE 2 (based on all Argo data, O) and OSSE 3 (combination of Argo and SOCAT data, X) provide
244 comparable results (Fig. 3b and c). OSSE 3 tends to have smaller uRMSD and bias and to lie closer to the STD
245 values from the NEMO/PISCES model (Fig. 4). OSSE 3 is based on the maximum of pseudo-observations for
246 training and represents most likely an unrealistic endmember. However, as mentioned before, OSSE 3 is used as
247 the benchmark to find other OSSEs with similar results and more feasible data coverage.

248
249 OSSE 4 (square) and OSSE 5 (rhombus) are based on OSSE 3, the only difference being the number of Argo
250 profiles: OSSE 3, 100%; OSSE 4, 25% and OSSE 5, 10%. The results of OSSEs 4 and 5 are similar to those
251 obtained for OSSE 3. The largest difference is observed over biome 17 (Fig. 3, Fig. 4i): correlation coefficients
252 are 0.85 (OSSE 3), 0.77 (OSSE 4), 0.75 (OSSE 5); biases are $-0.66 \mu\text{atm}$, $-2.25 \mu\text{atm}$, $-4.02 \mu\text{atm}$; uRMSDs are
253 $10.18 \mu\text{atm}$, $11.75 \mu\text{atm}$, $11.8 \mu\text{atm}$ (Tables 3, 4).

254
255 OSSEs 6 (triangle), 7 (inverted triangle), 8 (pentahedron) were trained on SOCAT data complemented with Argo
256 data in the Southern Hemisphere. In general, the skill scores are lower compared to OSSE 3, especially for OSSE
257 8 (10% of Argo data in the Southern Hemisphere) where results approach those of OSSE 1 (Fig. 3). Large
258 differences are obtained for biomes 12 and 17 (Fig. 3, Fig. 4e and i): in biome 12 and 17, correlation coefficients
259 for OSSE 6, 7, 8 are 0.64/0.86, 0.54/0.8, 0.52/0.66, respectively, compared to 0.79/0.85 for OSSE 3; uRMSDs are



260 11.46/10.01 μatm , 13.3/11.03 μatm , 13.87/15.16 μatm compared to 8/10.18 μatm for OSSE 3; biases are 3.82/
261 0.18 μatm , 3.77/-1.8 μatm , 2.7/-4.12 μatm compared to -0.14/-0.66 μatm for OSSE 3 (Tables 3, 4). Over biome
262 12 all OSSEs show STD values lower than the one computed for NEMO/PISCES model output (Table 3). This
263 could result from the STD of the mean output being slightly lower than the individual STDs for 4 OSSE FFNN
264 outputs (not shown). However, individual STDs also underestimate the NEMO/PISCES STD which might suggest
265 that the ensemble of predictors do not allow to properly represent the variability over the Equatorial Atlantic.
266

267 Reconstruction skill scores are improved by the addition of data from mooring stations to OSSEs 6, 7, and 8 in
268 OSSEs 9 (hexagon), 10 (star) and 11 (triangle centroid) (Fig. 3 and 4, Tables 3 and 4). Over the ensemble of 8
269 biomes the decrease in the number of Argo data goes along with a general decrease of correlation coefficients,
270 0.88 (OSSE 9), 0.85 (OSSE 10), 0.83 (OSSE 11), and an increase of uRMSDs, 8.37 μatm (OSSE 9), 8.71 μatm
271 (OSSE 10), 9.16 μatm (OSSE 11) (Fig. 3, 4a, Tables 3 and 4). Statistics are slightly worse for OSSE 11 compared
272 to OSSEs 9 and 10, which have comparable results. While OSSE 10 shows a smaller correlation coefficient over
273 the whole region compared to OSSE 9, its STD (24.89 μatm) lies closer to the NEMO/PISCES STD (25.34 μatm)
274 and it has a smaller bias (-0.39 μatm). Similar results are found over other biomes: in biome 12, OSSEs 9 and 10
275 have correlation coefficients close to each other (0.68 and 0.63, respectively) and larger than for OSSEs 6, 7 and
276 8, while for OSSE 11 it is 0.58. The STDs are almost equal (OSSE 9, 12.98 μatm and OSSE 10, 12.9 μatm) and
277 uRMSDs have a small difference compared to the one computed for OSSE 3 (8 μatm) (Tables 3, 4). Thus, the
278 remainder of the discussion will focus on OSSE 10 in comparison to OSSEs 1 and 3. OSSE 10 provides comparable
279 results to OSSE 9 and is in good agreement with OSSE 3 while using less data for training. Figures 3 and 4 are
280 summarized in Supplementary materials (Figure S1).
281

282 Figures 5a, b and c present the differences between reconstructed $p\text{CO}_2$ distributions (Fig.5 a – OSSE 1; b – OSSE
283 3; c – OSSE 10) and NEMO/PISCES output. The maximum in absolute value from 4 outputs for each OSSE FFNN
284 is shown (Eq. 4). There is a large improvement in the Southern Hemisphere for OSSEs 3 (Fig. 5b) and 10 (Fig.
285 5c) compared to OSSE 1 (Fig. 5a): the difference varies mostly between -3 and 3 μatm for OSSEs 3 and 10, and
286 between -15 and 15 μatm for OSSE 1 (Fig. 5). However, the average values of the mean over biomes are not
287 always better for OSSE 3 (Table 5): in biome 13, OSSE 1 shows a small positive difference of 0.11 μatm , while
288 for OSSE 3 negative differences of -0.32 μatm is computed, exceeding 0.11 μatm in its absolute value. This is due
289 to error compensation by averaging, the reduction of the positive difference in the middle of biome 13 in OSSE 3
290 increases the impact of negative small differences in this region. A large improvement is obtained in biomes 16
291 and 17: from -8.04 μatm for OSSE 1 to -1.89 μatm and -1.91 μatm for OSSEs 3 and 10 in biome 16, and from -
292 14.9 μatm for OSSE 1 to -2.05 μatm and -1.55 μatm for OSSEs 3 and 10 in biome 17 (Table 5). Over the whole
293 region, 70°W-30°E 80°S-80°N, OSSE 1 has a mean difference of -6.57 μatm , it is -1.7 μatm and -2.34 μatm for
294 OSSEs 3 and 10. The difference between OSSEs 3 and 10 results from the Labrador Sea and Baffin Bay: OSSE
295 10 has fewer data in this region compared to the OSSE 3. However, there is an improvement in OSSE 10 compared
296 to OSSE 1 and 3 in the Greenland Sea (Fig. 5). It results from the addition of mooring data in the Greenland Sea
297 region (Fig. 1c).
298

299 Figures 5d, e and f present the standard deviations (STD) of differences for all 4 outputs for each OSSE FFNN
300 (Fig.5 d – OSSE 1; e – OSSE 3; f – OSSE 10) (Eq. 5). Over most of the Atlantic Ocean STD varies between 0 and
301 10 μatm for OSSEs 3 and 10. In each case there is a strong STD along the coasts and in the Labrador Sea, as well
302 as the Baffin Bay. In general, the mean value of STD tends to decrease (Table 5) from OSSE 1 to OSSEs 3 and
303 10. In the Southern Hemisphere STD reaches up to 30 μatm (Figures 5d, e and f) when only SOCAT data are
304 used in the FFNN algorithm (OSSE 1). It is significantly reduced in response to the addition of float data in OSSEs
305 3 and 10 with also less spatial variability. The results for other OSSEs are added to the Supplementary material
306 (Table S2, Fig. S2, S3).
307

308 Figure 6 shows the correlation between the mean value of 4 OSSEs outputs and NEMO/PISCES $p\text{CO}_2$ (a - OSSE
309 1, b - OSSE 3, c - OSSE 10). The additional data from Argo floats and mooring stations increase the correlation
310 coefficient from 0.68 in the case of OSSE 1 (SOCAT data only) to 0.86 and 0.85 in the case of OSSEs 3 and 10
311 (Table 6). A higher correlation was also obtained for these two OSSEs compared to OSSE 1 over the region
312 covering the Greenland Sea, the Norwegian Sea and Barents Sea (mostly biome 9). In the Southern Hemisphere
313 the correlation with NEMO/PISCES $p\text{CO}_2$ is also larger when Argo data are included, especially in biomes 16 and
314 17: 0.7 and 0.57 for OSSE 1, 0.83 and 0.85 for OSSE 3, as well as 0.78 and 0.89 for OSSE 10 (Table 6). However,
315 there is a low correlation along the African coasts which is in agreement with our previous results for mean
316 difference and STD (Fig. 5). It reflects the predominantly open ocean data used for this exercise. A well-
317 pronounced decrease in correlation is observed for biome 15 (Subtropical seasonally stratified Southern Ocean).
318 Such a decrease can result from the spatial distribution of data or from the predictor data set. We will discuss it



319 further in the next section. The results for other OSSEs are presented in the Supplementary material (Table S3,
320 Fig. S4).

321
322 In Figure 7, time series of $p\text{CO}_2$ for OSSEs 1, 3 and 10 are compared to corresponding NEMO/PISCES model
323 output. For each OSSE, the mean $p\text{CO}_2$ from 4 FFNN outputs is shown, as well as the mean bias (OSSE -
324 NEMO/PISCES). Figure 7a and b presents the $p\text{CO}_2$ time series over the period of reconstruction 2008-2010 for
325 OSSE 1, 3, 10 compared to NEMO/PISCES $p\text{CO}_2$ used as reference (black) over all biomes. For OSSE 1 (SOCAT
326 data only) a large difference and an underestimation of reconstructed $p\text{CO}_2$ (blue) compared to NEMO/PISCES
327 $p\text{CO}_2$ (black) are found: the maximum error is up to $-10 \mu\text{atm}$ (Fig. 7b). To the contrary, OSSEs 3 and 10 show a
328 good agreement with NEMO/PISCES model output. Averages of $p\text{CO}_2$ over the 8 biomes are $372.18 \mu\text{atm}$ for
329 OSSE 3, $372.26 \mu\text{atm}$ for OSSE 10 and $368.39 \mu\text{atm}$ for OSSE 1, compared to $372.65 \mu\text{atm}$ for NEMO/PISCES
330 (Table 7). The experiment corresponding to the BGC-Argo distribution target over the entire Atlantic basin, OSSE
331 4 (Fig. S7, S8), has a basin-wide average $p\text{CO}_2$ equal to $371.8 \mu\text{atm}$ (Table 7). This corresponds to a larger
332 difference with NEMO/PISCES ($-0.84 \mu\text{atm}$) compared to OSSEs 3 and 10.

333
334 Panels (c) to (h) of Figure 7 illustrate time series of reconstructed $p\text{CO}_2$ for biomes with varying data coverage.
335 Biome 11, the Subtropical permanently stratified North Atlantic, (Figure 7c and d) is well covered by data. All
336 three OSSEs yield $p\text{CO}_2$ reconstructions that are in good accordance with the NEMO/PISCES reference. The
337 amplitude and the phasing of the seasonal cycle are well reproduced. The bias varies within a range of $\pm 5 \mu\text{atm}$
338 for OSSEs 3 and 10. A predominantly negative bias is found for OSSE 1 with values as high as $-10 \mu\text{atm}$. The
339 $p\text{CO}_2$ averaged over the total biome 11 area for OSSE 10 is close to NEMO/PISCES with, respectively 389.39
340 μatm and $390.11 \mu\text{atm}$ (Table 7). OSSE 1 yields a biome-averaged $p\text{CO}_2$ equal to $387.11 \mu\text{atm}$, while it is 389.39
341 μatm for the OSSE 3.

342
343 Biome 13, the Subtropical permanently stratified South Atlantic, (Figure 7e and f) corresponds to a region with a
344 low data coverage. We observe a large difference between $p\text{CO}_2$ reconstructed by OSSE 1 (blue) and
345 NEMO/PISCES (black). While the phasing of the reconstructed seasonal cycle is satisfying, it is noisy with a
346 systematic overestimation in spring by up to $18 \mu\text{atm}$ (Table 7). However, the total averaged $p\text{CO}_2$ over biome 13
347 for OSSE 1 is close to the one of NEMO/PISCES: $391.66 \mu\text{atm}$, respectively $389.54 \mu\text{atm}$. The preceding suggests
348 that while the variability of the predictors (mainly SST) is sufficient to constrain at first order the biome-average
349 $p\text{CO}_2$ and the phasing of the seasonal cycle, an improved coverage by *in situ* observations is needed for a smooth
350 reconstruction of the seasonal cycle's amplitude. Reconstructions are largely improved by the addition of data
351 from Argo floats (OSSE 3) and moorings (OSSE 10). Biases mostly range between -3 and $3 \mu\text{atm}$ for these OSSEs.
352 The Southern Ocean Ice biome (biome 17) is characterized by a sparse data coverage and a bias towards the ice-
353 free season. The results for biome 17 are presented in Figure 7g and h. OSSE 1 underestimates the $p\text{CO}_2$ in this
354 region over the full seasonal cycle. The biome-wide average is $351.44 \mu\text{atm}$, $-11.63 \mu\text{atm}$ below the
355 NEMO/PISCES reference. The reconstruction is much improved for OSSEs 3 and 10, both for the phasing and
356 amplitude of the seasonal cycle, as well as for the biome-wide averages. The latter are $362.42 \mu\text{atm}$ and 362.87
357 μatm , respectively for OSSE 3 and OSSE 10, compared to $363.08 \mu\text{atm}$ computed for NEMO/PISCES (Table 7)
358 Results for all OSSEs and for all biomes are included to the Supplementary material (Table S4, Fig. S5 - S10).

359
360 Figure 8 shows the sea-air CO_2 flux time series (negative, uptake of CO_2 by the ocean). Over all biomes in the
361 region $70^\circ\text{W}-30^\circ\text{E}$ $80^\circ\text{S}-80^\circ\text{N}$ the OSSEs 3 (red) and 10 (green) show a good agreement with NEMO/PISCES
362 $f_g\text{CO}_2$: the differences vary around zero and mostly do not exceed $\pm 0.3 \text{ Pg/yr}$ (Fig. 8b, d, f and h). The total
363 averaged $f_g\text{CO}_2$ for OSSE 3 and 10 are -0.74 Pg/yr compared to -0.7 Pg/yr in NEMO/PISCES, while for OSSE 1
364 it equals -0.99 Pg/yr (Table 8). The mean value over biome 11 is slightly better for OSSE 10 than for OSSE 3
365 compared to NEMO/PISCES: -0.06 Pg/yr (OSSE 10), -0.07 (OSSEs 3) and -0.03 Pg/yr for NEMO/PISCES. The
366 OSSE 1 (blue) shows again a large difference, it overestimates the ocean sink computed by the NEMO/PISCES
367 model mostly during the whole period (Fig. 8b). In the well data-covered biome 11, OSSE 1 also has a tendency
368 to overestimate the sea-air CO_2 flux (Fig. 8d): the total averaged $f_g\text{CO}_2$ is -0.18 Pg/yr for OSSE 1 while it is -0.03
369 Pg/yr in the model. While the phasing and amplitude of the seasonal cycle of sea-air fluxes of CO_2 are well
370 reproduced over biome 13 by OSSEs 3 and 10, the $f_g\text{CO}_2$ reconstructed by OSSE 1 is noisy with differences with
371 respect to the model reference of up to 1 Pg/yr (Fig. 8e). The biome-wide mean sea-air flux of CO_2 is close to zero
372 in NEMO/PISCES: -0.004 Pg/yr . This slight uptake of CO_2 by the ocean in the model reference is not reproduced
373 by the OSSEs which yield a source over biome 13, albeit of variable strength: 0.19 Pg/yr for OSSE 1, 0.05 Pg/yr
374 for OSSE 3 and 0.08 Pg/yr for OSSE 10. Over the Southern Ocean biome 17 (Fig. 8g and h) OSSE 1 (blue)
375 overestimates $f_g\text{CO}_2$ by -0.65 Pg/yr (Table 8). OSSE 10 (green) reproduces the local maxima and minima of the
376 $f_g\text{CO}_2$ time series slightly better than OSSE 3, with average differences equaling -0.03 Pg/yr and -0.06 Pg/yr ,
377 respectively. Results for all OSSEs and for all biomes can be found in the Supplementary material (Table S5, Fig.
378 S11 - S16).



379
380 The relationship between the average number of Argo floats (5-day period) and the error in $fgCO_2$ estimates (Table
381 8, Table S5) is shown in Figure 9 for all biomes (a), biome 11 (b), biome 13 (c) and biome 17 (d). Figure 9a
382 illustrates how the increase of the number of floats usually yields a reduction in the error of $fgCO_2$ estimates.
383 Considering the whole region, OSSE 10 provides the best results with less Argo floats (-0.04 PgC/yr and 48 Argo
384 floats). At the biome-scale, the addition of floats does, however, not systematically reduce the error. This holds
385 for biome 11 (Fig. 9b), which is well-covered by observations, but also for biome 13 with a much sparser data-
386 coverage (Fig. 9d). For biome 11, OSSE 10 has the best trade-off between error reduction and number of floats.
387 The largest error (0.22 PgC/yr) is obtained for OSSE 2 (only Argo data). It suggests that the period chosen for this
388 study is too short to adequately capture the seasonal variability. This hypothesis is supported by the fact that while
389 OSSE 3 and OSSE 2 share the same number of Argo data, OSSE 3 is further constrained by SOCAT data that
390 cover the period 2001-2010. These additional data from SOCAT introduce the information needed for the
391 reconstruction of the seasonal cycle. For biome 13 (Fig. 9c), the combination of SOCAT data and Argo float data
392 improves estimates of $fgCO_2$. The errors in OSSE 10 are comparable to OSSE 3 (benchmark), 0.08 PgC/yr (OSSE
393 10) and 0.06 PgC/yr (OSSE 3). The error is even lower for OSSE 11 (0.04 PgC/yr), the experiment with the
394 smallest number of Argo floats (19), than for OSSE 3. Unfortunately, results provided by OSSE 11 are less good
395 over the remainder of the biomes. The tendency for a decrease of $fgCO_2$ error with an increase of the number of
396 Argo floats is confirmed for biome 17 (Fig. 9d). The additional data from mooring stations (OSSE 9, 10 and 11)
397 improve in particular OSSEs with smaller numbers of floats. An error of -0.03 PgC/yr is computed for OSSE 10
398 (49 floats) over biome 17. The results for other biomes can be found in the Supplementary material (Fig. S17).

399 4 Summary and Conclusion

400 The aim of this work was to identify an optimal observational network of pCO_2 over the Atlantic Ocean. The
401 analysis was based on results obtained with a Feed-Forward Neural Network model trained on the SOCAT
402 database. The SOCAT database has a sparse coverage in the Southern Hemisphere. The approach consisted in
403 adding the position of mooring data and Argo trajectories in the Atlantic Ocean to find an optimal distribution and
404 combination of data to reconstruct pCO_2 with a good accuracy. The advantage of the SOCAT database is the long
405 time period covered by its records, which allows to reconstruct the interannual variability with a good accuracy.
406 However, its data coverage is biased towards the North Atlantic, which leads to larger reconstruction errors over
407 the South Atlantic by the Neural Network. As a long-term perspective, the inclusion of data from Argo floats will
408 contribute to a more homogenous data distribution and provide a better spatial coverage. The Argo floats and
409 moorings used here do not currently provide pCO_2 measurements, hence only their positions were used to build
410 OSSEs. A series of experiments were performed using outputs from the NEMO/PISCES model. The model
411 simulations were sub-sampled at co-localized sites of observing systems for all predictors (SSS, SST, SSH, CHL,
412 MLD, $pCO_{2, atm}$) used in the FFNN and the target (pCO_2) to create pseudo-observations with a 5-day time step.
413 These experiments should be useful for the planning of future deployments of BGC-Argo floats (Biogeochemical-
414 Argo Planning Group, 2016) and moorings equipped with the sensors to measure pCO_2 or CO_2 fugacity.
415

416 The results suggest that the addition of data from Argo floats could significantly improve the accuracy of FFNN-
417 based ocean pCO_2 reconstructions over the Atlantic Ocean and the Atlantic sector of the Southern Ocean compared
418 to the case when only SOCAT data are used (OSSE 1). However, even with an improved coverage over the open
419 ocean, additional observations are required in coastal regions and shelf seas which are not accessible to floats, as
420 well as in regions with a strong seasonal variability of pCO_2 and all predictors. This is exemplified by OSSE 2,
421 the experiment based on all Argo data, which yields high RMSDs in biome 9, the Subpolar seasonally stratified
422 North Atlantic (Fig. 3, Fig.4b, Table 4). The RMSD of 17.1 μatm reflects the poor coverage of this region by Argo
423 floats (Fig. 1b), in particular the Greenland Sea and the North Sea, with a large part of the latter not suitable for
424 the deployment of floats. The combination of SOCAT data and Argo floats (OSSE 3) improves the reconstruction
425 with a RMSD reduced to 9.59 μatm (Fig. 4b, Table 4).

426 The reduction of the number of Argo data used in our experiments slightly decreases the accuracy (Fig. 3 and 4,
427 Tables 3 and 4). A lower number of Argo data corresponds, however, to a more realistic distribution of instruments
428 and to the target of the global BGC-Argo network. The results are still comparable to OSSE 3. The best
429 compromise between the statistics yielded by the comparison between reconstructed pCO_2 and NEMO/PISCES
430 outputs, as well as the feasibility of a future observation network is found for OSSE 10. In this experiment SOCAT
431 data are combined with simulated mooring data and 25% of the initial distribution of Argo floats placed only in
432 the Southern Hemisphere (around 49 floats with a 5-day sampling period). The use of only SOCAT data results in
433 a correlation coefficient of 0.67 compared to NEMO/PISCES output and a standard deviation of 26.08 μatm (25.34
434 μatm for NEMO/PISCES) over the region of study. While the successful OSSE 10 has a correlation coefficient of
435 0.85 and a standard deviation of 24.89 μatm . These results are close to the unrealistic benchmark case with total



436 and only Argo float distribution over 2008-2010: 0.87 and 23.79 μatm . The total $p\text{CO}_2$ over the whole region is
437 also close to NEMO/PISCES, $\sim 370\ \mu\text{atm}$ and $\sim 371\ \mu\text{atm}$, respectively. The air-sea flux $f_g\text{CO}_2$ is -0.83 Pg/yr
438 (OSSE) and -0.76 Pg/yr (NEMO). OSSE 10 shows the bias reduction of derived estimates of sea-air CO_2 fluxes
439 by 74% from OSSE 1 ($f_g\text{CO}_2$ is -1.03 Pg/yr) compared to NEMO/PISCES.

440 The OSSE 10 network could be further improved by instrumenting the Baffin Bay, the Labrador Sea, the
441 Norwegian Sea, as well as regions along the coast of Africa (10°N to 20°S), all regions with pronounced biases in
442 all OSSEs, with moorings or gliders along the shelf break and on the continental shelf.

443
444 The inclusion of errors from *in situ* measurements is one of the next steps of this work. It will include the errors
445 for predictor values (SSS, SST, SSH, CHL, MLD, $p\text{CO}_{2,\text{atm}}$) that are measured directly or derived from remote
446 sensing (e.g., SST, chlorophyll, SSH), as well as the errors related to the computation of $p\text{CO}_2$ from pH and
447 alkalinity. The new FFNN runs could provide important information on the effect of biases from observational
448 datasets and identify predictors or targets that have large errors and that must be corrected.
449

450 Author contribution:

451 ADS, MG, MV contributed to the development of the methodology and designed the experiments, and ADS
452 carried them out. ADS developed the model code and performed the simulations. ADS prepared the paper with
453 contributions from all coauthors.

454 Acknowledgments:

455 This study was funded by the AtlantOS project (EU Horizon 2020 research and innovation program, grant
456 agreement no. 2014-633211) and GreenGrog PPR (GMMC). At present ADS is under funding from the Royal
457 Society (grant no. RP\R1\191063) at the UEA. MV acknowledges support from the CoCliServ project, which is
458 part of ERA4CS, an ERA-NET initiated by JPI Climate and cofunded by the European Union. Authors thanks
459 Florent Gasparin for his help with reference data of Argo distribution.
460

461 References

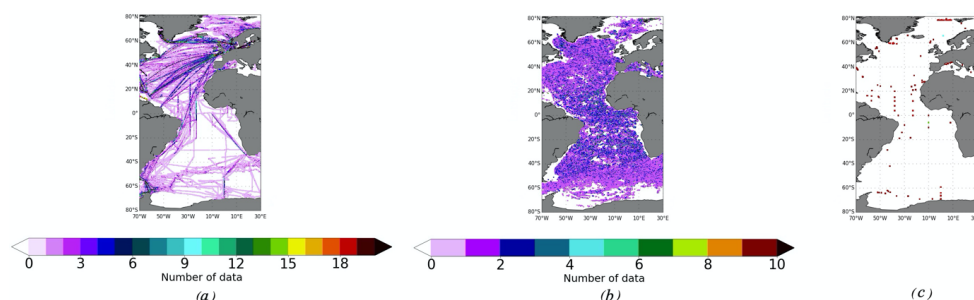
- 462
463 Aumont, O., and L. Bopp: Globalizing results from ocean in situ iron fertilization studies, *Global Biogeochem.*
464 *Cycles*, 20, GB2017, doi:10.1029/2005GB002591, 2006.
465
466 Bakker, D. C. E., Pfeil, B., Landa, C. S., Metzl, N., O'Brien, K. M., Olsen, A., Smith, K., Cosca, C., Harasawa, S.,
467 Jones, S. D., Nakaoka, S.-I., Nojiri, Y., Schuster, U., Steinhoff, T., Sweeney, C., Takahashi, T., Tilbrook, B.,
468 Wada, C., Wanninkhof, R., Alin, S. R., Balestrini, C. F., Barbero, L., Bates, N. R., Bianchi, A. A., Bonou, F.,
469 Boutin, J., Bozec, Y., Burger, E. F., Cai, W.-J., Castle, R. D., Chen, L., Chierici, M., Currie, K., Evans, W.,
470 Featherstone, C., Feely, R. A., Fransson, A., Goyet, C., Greenwood, N., Gregor, L., Hankin, S., Hardman-
471 Mountford, N. J., Harlay, J., Hauck, J., Hoppema, M., Humphreys, M. P., Hunt, C. W., Huss, B., Ibáñez, J. S. P.,
472 Johannessen, T., Keeling, R., Kitidis, V., Körtzinger, A., Kozyr, A., Krasakopoulou, E., Kuwata, A., Landschützer,
473 P., Lauvset, S. K., Lefèvre, N., Lo Monaco, C., Manke, A., Mathis, J. T., Merlivat, L., Millero, F. J., Monteiro, P.
474 M. S., Munro, D. R., Murata, A., Newberger, T., Omar, A. M., Ono, T., Paterson, K., Pearce, D., Pierrot, D.,
475 Robbins, L. L., Saito, S., Salisbury, J., Schlitzer, R., Schneider, B., Schweitzer, R., Sieger, R., Skjelvan, I.,
476 Sullivan, K. F., Sutherland, S. C., Sutton, A. J., Tadokoro, K., Telszewski, M., Tuma, M., van Heuven, S. M. A.
477 C., Vandemark, D., Ward, B., Watson, A. J., and Xu, S.: A multi-decade record of high-quality $f\text{CO}_2$ data in
478 version 3 of the Surface Ocean CO_2 Atlas (SOCAT), *Earth Syst. Sci. Data*, 8, 383–413,
479 <https://doi.org/10.5194/essd-8-383-2016>, 2016.
480
481 Biogeochemical-Argo Planning Group: The scientific rationale, design and Implementation Plan for a
482 Biogeochemical-Argo float array. Edited by Ken Johnson and Hervé Claustre. doi:10.13155/46601, 2016.
483
484 Bishop, C. M.: *Neural Networks for Pattern Recognition*, Oxford University Press, Cambridge, UK, 1995.
485
486 Bittig, H.C., Steinhoff, T., Claustre, H., Fiedler, B., Williams, N.L., Sauzède, R., Körtzinger, A., and Gattuso, J.-
487 P.: An Alternative to Static Climatologies: Robust Estimation of Open Ocean CO_2 Variables and Nutrient



- 488 Concentrations From T, S, and O₂ Data Using Bayesian Neural Networks, *Front. Mar. Sci.*, 5, 328,
489 <https://doi.org/10.3389/fmars.2018.00328>, 2018.
- 490 Bushinsky, S. M., Landschützer, P., Rödenbeck, C., Gray, A. R., Baker, D., Mazloff, M. R., et al.: Reassessing
491 Southern Ocean air-sea CO₂ flux estimates with the addition of biogeochemical float observations, *Global*
492 *Biogeochemical Cycles*, 33, 1370–1388, <https://doi.org/10.1029/2019GB006176>, 2019.
- 493 Chollet, F.: Keras, available at: <https://keras.io> (last access: 12 May 2019), 2015.
- 494 Ciais, P., Sabine, C., Bala, G., Bopp, L., Brovkin, V., Canadell, J., Chhabra, A., DeFries, R., Galloway, J.,
495 Heimann, M., Jones, C., Le Quéré, C., Myneni, R. B., Piao, S., and Thornton, P.: Carbon and other biogeochemical
496 cycles, in: *Climate Change 2013: The Physical Science Basis. Contribution of Working Group I to the Fifth*
497 *Assessment Report of the Intergovernmental Panel on Climate Change*, edited by: Stocker, T. F., Qin, D., Plattner,
498 G.-K., Tignor, M., Allen, S. K., Boschung, J., Nauels, A., Xia, Y., Bex, V., and Midgley, P. M., Cambridge
499 University Press, Cambridge, United Kingdom and New York, NY, USA, 2013.
- 500
501 Denvil-Sommer, A., Gehlen, M., Vrac, M., and Mejia, C.: LSCE-FFNN-v1: a two-step neural network model for
502 the reconstruction of surface ocean pCO₂ over the global ocean, *Geosci. Model Dev.*, 12, 2091–2105,
503 <https://doi.org/10.5194/gmd-12-2091-2019>, 2019.
- 504
505 Fay, A. R. and McKinley, G. A.: Global open-ocean biomes: mean and temporal variability, *Earth Syst. Sci.*
506 *Data*, 6, 273–284, <https://doi.org/10.5194/essd-6-273-2014>, 2014.
- 507
508 Fay, A. R., McKinley, G. A., and Lovenduski, N. S.: Southern Ocean carbon trends: Sensitivity to methods,
509 *Geophys. Res. Lett.*, 41, 6833–6840, <https://doi.org/10.1002/2014GL061324>, 2014.
- 510
511 Friedlingstein, P., O'Sullivan, M., Jones, M. W., Andrew, R. M., Hauck, J., Olsen, A., Peters, G. P., Peters, W.,
512 Pongratz, J., Sitch, S., Le Quéré, C., Canadell, J. G., Ciais, P., Jackson, R. B., Alin, S., Aragão, L. E. O. C., Armeth,
513 A., Arora, V., Bates, N. R., Becker, M., Benoit-Cattin, A., Bittig, H. C., Bopp, L., Bultan, S., Chandra, N.,
514 Chevallier, F., Chini, L. P., Evans, W., Florentie, L., Forster, P. M., Gasser, T., Gehlen, M., Gilfillan, D., Gkritzalis,
515 T., Gregor, L., Gruber, N., Harris, I., Hartung, K., Haverd, V., Houghton, R. A., Ilyina, T., Jain, A. K., Joetzjer,
516 E., Kadono, K., Kato, E., Kitidis, V., Korsbakken, J. I., Landschützer, P., Lefèvre, N., Lenton, A., Lienert, S., Liu,
517 Z., Lombardozzi, D., Marland, G., Metzler, N., Munro, D. R., Nabel, J. E. M. S., Nakaoka, S.-I., Niwa, Y., O'Brien,
518 K., Ono, T., Palmer, P. I., Pierrot, D., Poulter, B., Resplandy, L., Robertson, E., Rödenbeck, C., Schwinger, J.,
519 Séférian, R., Skjelvan, I., Smith, A. J. P., Sutton, A. J., Tanhua, T., Tans, P. P., Tian, H., Tilbrook, B., van der
520 Werf, G., Vuichard, N., Walker, A. P., Wanninkhof, R., Watson, A. J., Willis, D., Wiltshire, A. J., Yuan, W., Yue,
521 X., and Zaehle, S.: *Global Carbon Budget 2020*, *Earth Syst. Sci. Data*, 12, 3269–3340,
522 <https://doi.org/10.5194/essd-12-3269-2020>, 2020.
- 523
524 Gasparin, F., Guinehut, S., Mao, C., Mirouze, I., Rémy, E., King, R.R., Hamon, M., Reid, R., Storto, A., Le Traon,
525 P.Y. and Martin, M.J.: Requirements for an integrated in situ Atlantic Ocean observing system from coordinated
526 observing system simulation experiments, *Frontiers in Marine Science*, 6, p.83, 2019.
- 527
528 Gehlen, M., Berthet, S., Séférian, R., Ethé, C., and Penduff, T.: Quantification of chaotic intrinsic variability of
529 sea-air CO₂ fluxes at interannual timescales, *Geophysical Research Letters*, 47, e2020GL088304,
530 <https://doi.org/10.1029/2020GL088304>, 2020.
- 531
532 Gould, J., Roemmich, D., Wijffels, S., Freeland, H., Ignaszewsky, N., Jianping, X., et al.: Argo profiling floats
533 bring new era of in situ ocean observations, *Eos Transactions American Geophysical Union*, 85(19): 185–19,
534 <https://doi.org/10.1029/2004EO190002>, 2004.
- 535
536 Gregor, L., Lebehot, A. D., Kok, S., and Scheel Monteiro, P. M.: A comparative assessment of the uncertainties
537 of global surface ocean CO₂ estimates using a machine-learning ensemble (CSIR-ML6 version 2019a) – have we
538 hit the wall? *Geosci. Model Dev.*, 12, 5113–5136, <https://doi.org/10.5194/gmd-12-5113-2019>, 2019.
- 539
540 Hauck, J., Zeising, M., Le Quéré, C., Gruber, N., Bakker, D.C.E., Bopp, L., Chau, T.T.T., Gürses, Ö., Ilyina, T.,
Landschützer, P., Lenton, A., Resplandy, L., Rödenbeck, C., Schwinger, J., and Séférian, R.: Consistency and

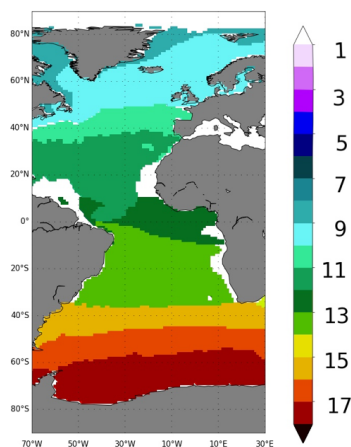


- 541 Challenges in the Ocean Carbon Sink Estimate for the Global Carbon Budget, *Front. Mar. Sci.* 7:571720. doi:
542 10.3389/fmars.2020.571720, 2020.
543
- 544 Landschützer, P., Gruber, N., Bakker, D. C. E., Schuster, U., Nakaoka, S., Payne, M. R., Sasse, T. P., and Zeng,
545 J.: A neural network-based estimate of the seasonal to inter-annual variability of the Atlantic Ocean carbon sink,
546 *Biogeosciences*, 10, 7793–7815, <https://doi.org/10.5194/bg-10-7793-2013>, 2013.
- 547 Landschützer, P., Gruber, N., and Bakker, D. C. E.: Decadal variations and trends of the global ocean carbon sink,
548 *Global Biogeochem. Cy.*, 30, 1396–1417, <https://doi.org/10.1002/2015GB005359>, 2016.
- 549 Nakaoka, S., Telszewski, M., Nojiri, Y., Yasunaka, S., Miyazaki, C., Mukai, H., and Usui, N.: Estimating temporal
550 and spatial variation of ocean surface $p\text{CO}_2$ in the North Pacific using a self-organizing map neural network
551 technique, *Biogeosciences*, 10, 6093–6106, <https://doi.org/10.5194/bg-10-6093-2013>, 2013.
- 552 Rödenbeck, C., Bakker, D. C. E., Metzl, N., Olsen, A., Sabine, C., Cassar, N., Reum, F., Keeling, R. F., and
553 Heimann, M.: Interannual sea–air CO_2 flux variability from an observation-driven ocean mixed-layer scheme,
554 *Biogeosciences*, 11, 4599–4613, <https://doi.org/10.5194/bg-11-4599-2014>, 2014.
- 555 Rödenbeck, C., Bakker, D. C. E., Gruber, N., Iida, Y., Jacobson, A. R., Jones, S., Landschützer, P., Metzl, N.,
556 Nakaoka, S., Olsen, A., Park, G.-H., Peylin, P., Rodgers, K. B., Sasse, T. P., Schuster, U., Shutler, J. D., Valsala,
557 V., Wanninkhof, R., and Zeng, J.: Data-based estimates of the ocean carbon sink variability – first results of the
558 Surface Ocean $p\text{CO}_2$ Mapping intercomparison (SOCOM), *Biogeosciences*, 12, 7251–7278,
559 <https://doi.org/10.5194/bg-12-7251-2015>, 2015.
- 560 Rumelhart, D. E., Hinton, G. E., and Williams, R. J.: Learning internal representations by backpropagating errors,
561 *Nature*, 323, 533–536, 1986.
562
- 563 Schuster, U., McKinley, G. A., Bates, N., Chevallier, F., Doney, S. C., Fay, A. R., González-Dávila, M., Gruber,
564 N., Jones, S., Krijnen, J., Landschützer, P., Lefèvre, N., Manizza, M., Mathis, J., Metzl, N., Olsen, A., Rios, A. F.,
565 Rödenbeck, C., Santana-Casiano, J. M., Takahashi, T., Wanninkhof, R., and Watson, A. J.: An assessment of the
566 Atlantic and Arctic sea–air CO_2 fluxes, 1990–2009, *Biogeosciences*, 10, 607–627, <https://doi.org/10.5194/bg-10-607-2013>, 2013.
567
- 568 Takahashi, T., Sutherland, S. C., Sweeney, C., Poisson, A., Metzl, N., Tilbrook, B., Bates, N., Wanninkhof, R.,
569 Feely, R. A., Sabine, C., Olafsson, J., and Nojiri, Y.: Global sea–air CO_2 flux based on climatological surface ocean
570 $p\text{CO}_2$, and seasonal biological and temperature effects, *Deep-Sea Res. Pt. II*, 49, 1601–1622,
571 [https://doi.org/10.1016/S0967-0645\(02\)00003-6](https://doi.org/10.1016/S0967-0645(02)00003-6), 2002.
572
- 573 Takahashi, T., Sutherland, S. C., Wanninkhof, R., Sweeney, C., Feely, R. A., Chipman, D. W., Hales, B.,
574 Friederich, G., Chavez, F., Sabine, C., Watson, A., Bakker, D. C. E., Schuster, U., Metzl, N., Yoshikawa-Inoue,
575 H., Ishii, M., Midorikawa, T., Nojiri, Y., Körtzinger, A., Steinhoff, T., Hoppema, M., Olafsson, J., Arnarson, T.
576 S., Tilbrook, B., Johannessen, T., Olsen, A., Bellerby, R., Wong, C. S., Delille, B., Bates, N. R., and de Baar, H.
577 J. W.: Climatological mean and decadal change in surface ocean $p\text{CO}_2$, and net sea–air CO_2 flux over the global
578 oceans, *Deep-Sea Res. Pt. II*, 56, 554–577, <https://doi.org/10.1016/j.dsr2.2008.12.009>, 2009.
- 579 Terhaar, J., Orr, J. C., Gehlen, M., Ethé, C., and Bopp, L.: Model constraints on the anthropogenic carbon budget
580 of the Arctic Ocean, *Biogeosciences*, 16, 2343–2367, <https://doi.org/10.5194/bg-16-2343-2019>, 2019.
- 581 Williams, N. L., et al.: Calculating surface ocean $p\text{CO}_2$ from biogeochemical Argo floats equipped with pH: An
582 uncertainty analysis, *Global Biogeochem. Cycles*, 31, 591–604, doi:10.1002/2016GB005541, 2017.
583
- 584 Zeng, J., Nojiri, Y., Landschützer, P., Telszewski, M., and Nakaoka, S.: A global surface ocean $f\text{CO}_2$ climatology
585 based on a feed-forward neural network, *J. Atmos. Ocean Technol.*, 31, 1838–1849,
586 <https://doi.org/10.1175/JTECH-D-13-00137.1>, 2014.
587



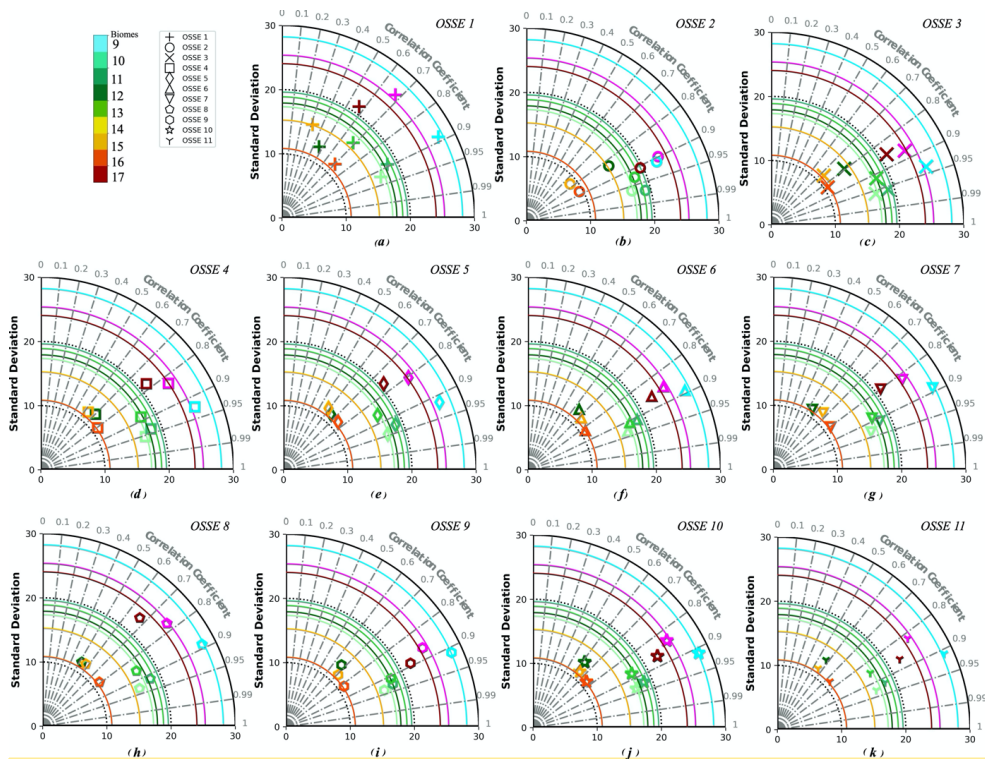
588
589
590
591

Figure 1: Spatial distribution of data sets used for training (number of measurements per grid points): (a) SOCAT data (5-day time step) for the period 2001-2010; (b) Argo data (5-day time step) for the period 2008-2010; (c) mooring positions modelled for the period 2008-2010 (5-day time step).



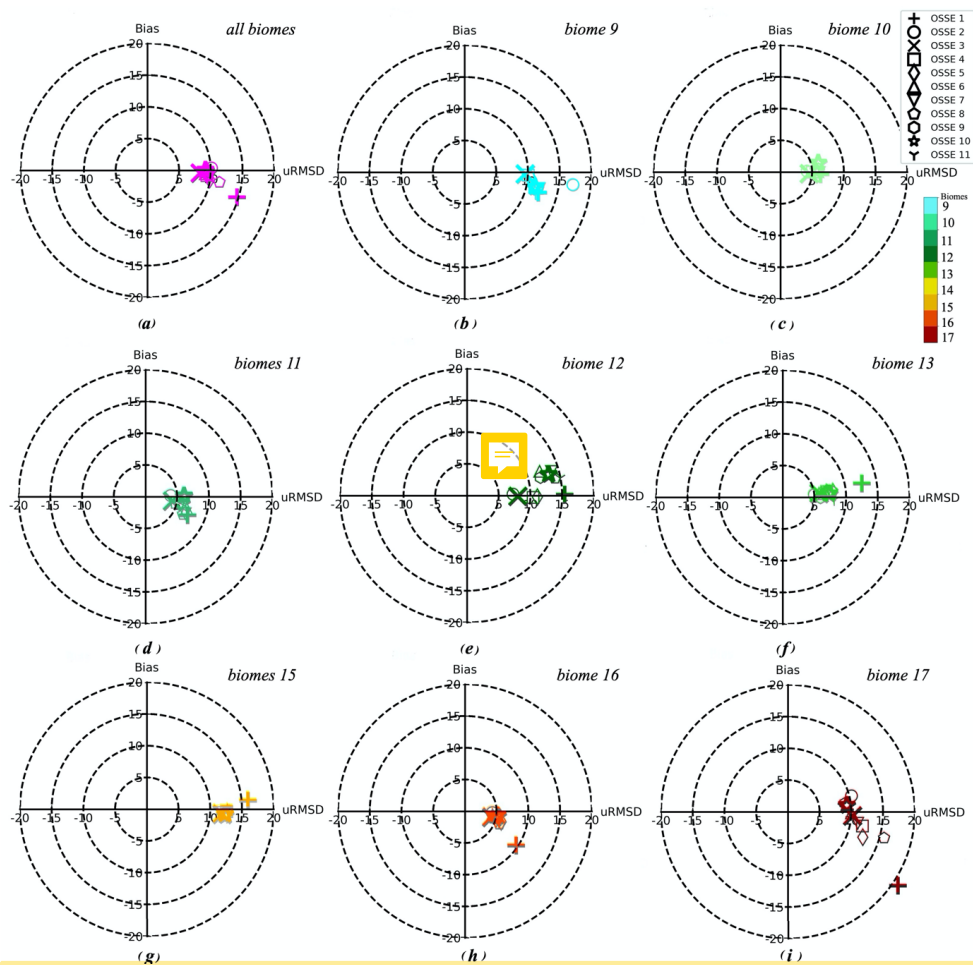
592
593
594

Figure 2: Map of biomes (after Rödenbeck et al., 2015; Fay and McKinley, 2014) focused on the region [70°W-30°E] and used for comparison between OSSEs.



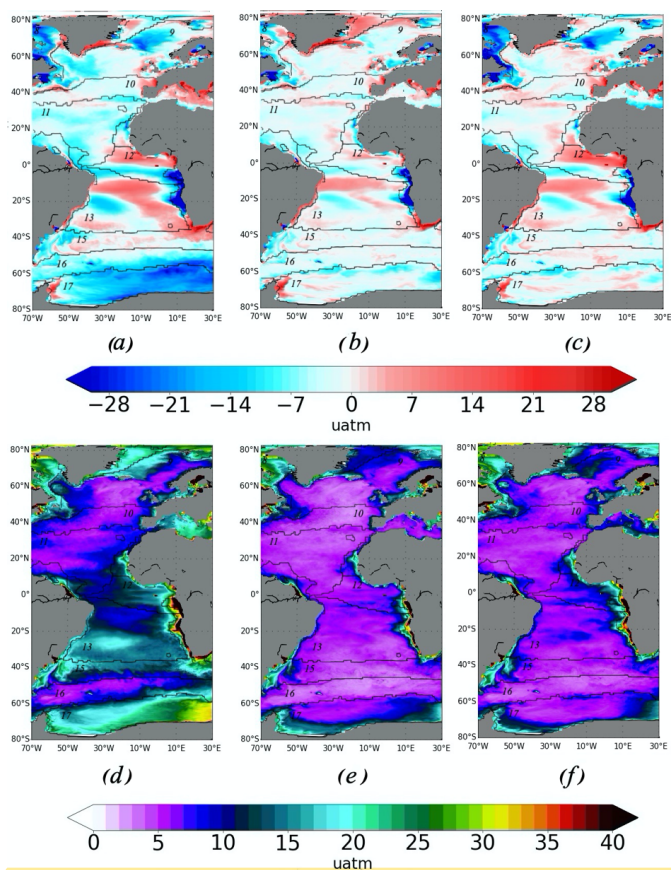
595
 596
 597
 598

Figure 3: Taylor Diagram of 11 OSSEs summarized in Table 2; colour code corresponds to Fig. 2: (a) - OSSE 1; (b) - OSSE 2; (c) - OSSE 3; (d) - OSSE 4; (e) - OSSE 5; (f) - OSSE 6; (g) - OSSE 7; (h) - OSSE 8; (i) - OSSE 9; (j) - OSSE 10; (k) - OSSE 11.



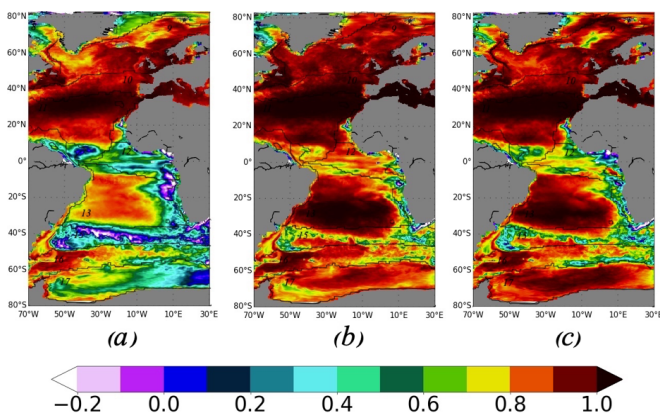
599
 600
 601

Figure 4: Target Diagram per biome for 11 OSSEs: (a) - all 8 biomes, (b) - biome 9, (c) - biome 10, (d) - biome 11, (e) - biome 12, (f) - biome 13, (g) - biome 15, (h) - biome 16, (i) - biome 17.



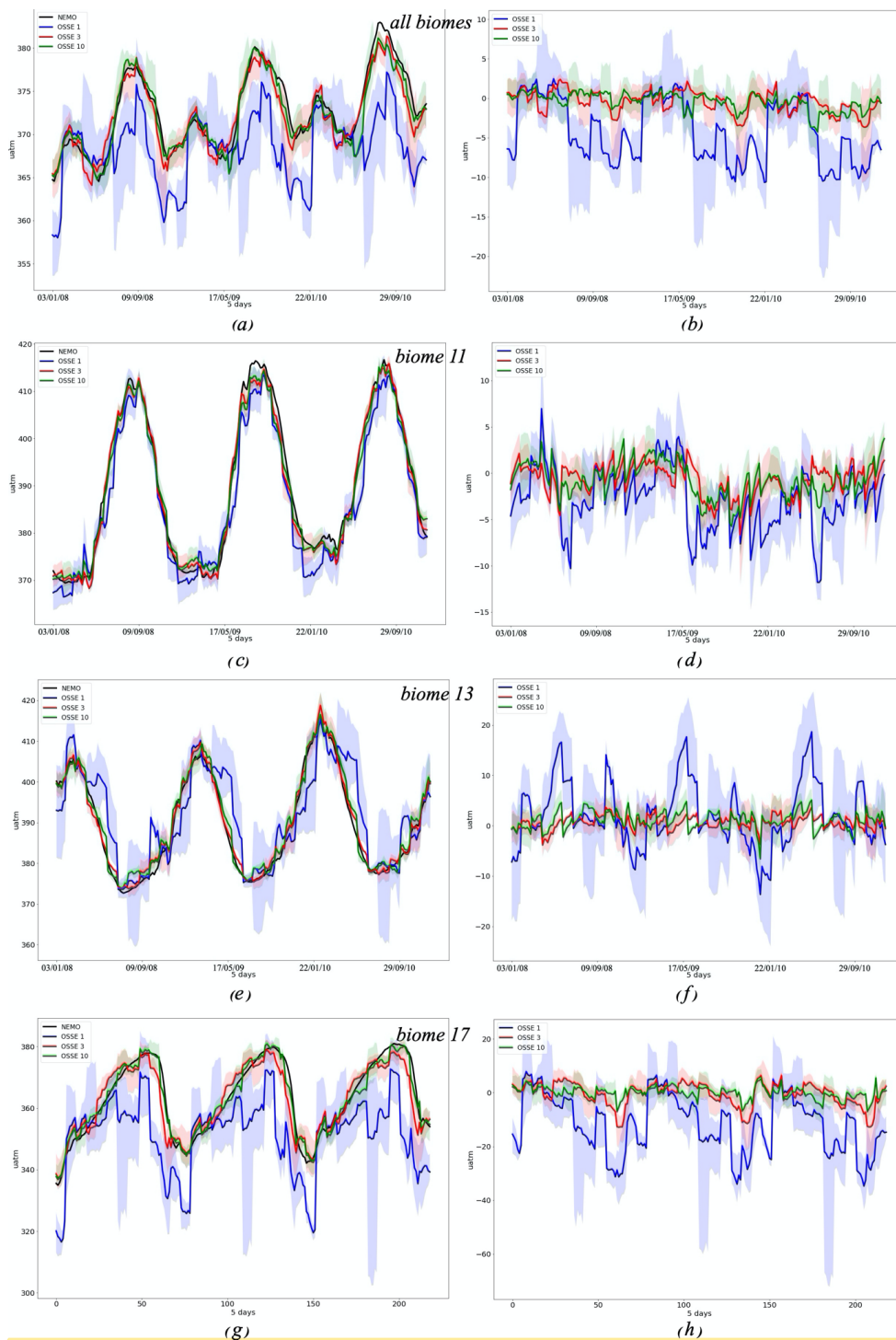
602
 603
 604
 605
 606

Figure 5: Differences between OSSE FFNN outputs and NEMO/PISCES $p\text{CO}_2$ and its standard deviation (STD) in μatm : (a), (b), (c) - its maximum in absolute value (maximum bias) from 4 outputs for each OSSE FFNN, Eq. (4); (g), (h) - standard deviation of differences for all 4 outputs for each OSSE FFNN, Eq. (5). (a), (d) – OSSE 1; (b), (e) – OSSE 3; (c), (f) – OSSE 10.



607
 608
 609
 610

Figure 6: Correlation coefficient between OSSE FFNN outputs and NEMO/PISCES $p\text{CO}_2$: (a) - OSSE 1, (b) - OSSE 3, (c) - OSSE 10.

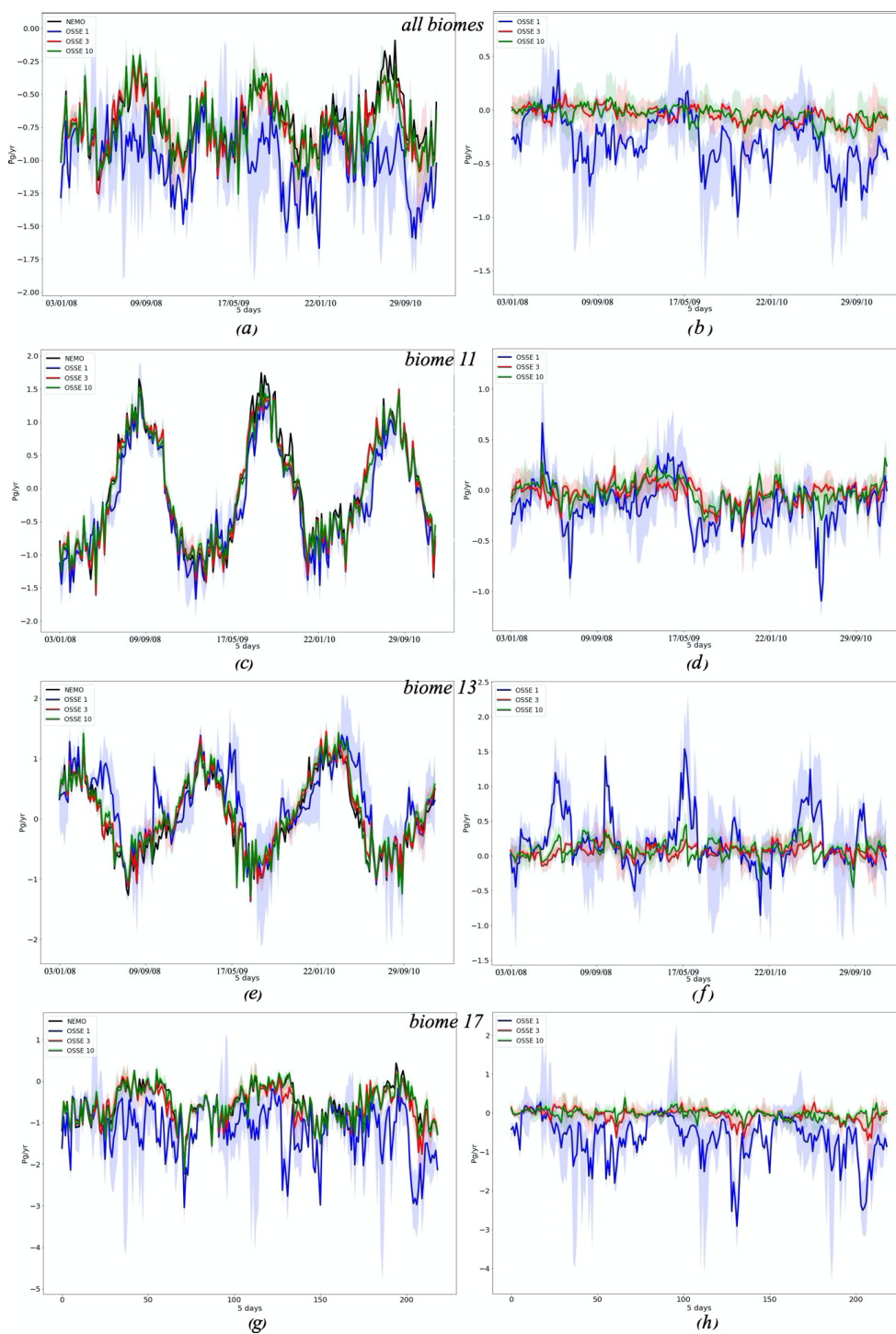


611
 612
 613

Figure 7: (a), (c), (e) - mean of 4 FFNN outputs for OSSE 1 (blue), 3 (red), 10 (green); shadow is the maximum and minimum values from 4 FFNN outputs for each OSSE. Black curve - NEMO/PISCES $p\text{CO}_2$. (b), (d), (f) - mean of



614 differences between OSSE 1 (blue), 3 (red), 10 (green) of 4 FFNN outputs and NEMO/PISCES $p\text{CO}_2$; shadow is the
615 maximum and minimum values of differences from 4 FFNN outputs for each OSSE. (a), (b) - estimates are available
616 over all biomes presented in Figure 2 except biome 8; (c), (d) - biome 11; (e), (f) - biome 13; (g), (h) - biome 17.



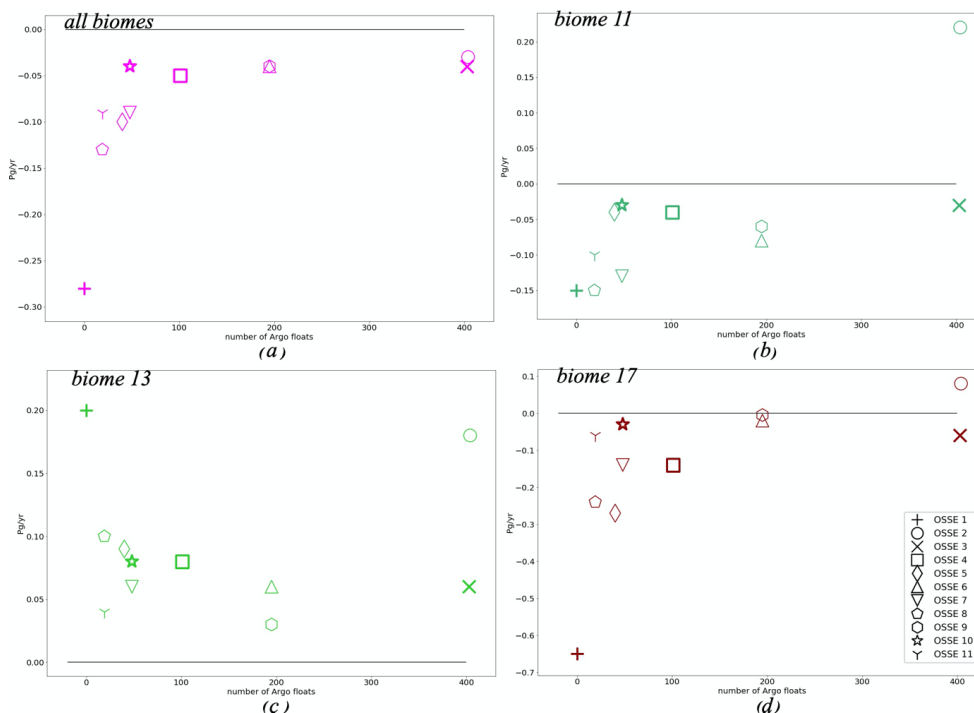
617

618
 619

Figure 8: (a), (c), (e) - mean of sea-air CO₂ flux from 4 FFNN outputs for OSSE 1 (blue), 3 (red), 10 (green); shadow is the maximum and minimum values from 4 FFNN sea-air CO₂ flux estimates for each OSSE. Black curve -



620 NEMO/PISCES $fgCO_2$. (b), (d), (f) - mean of differences between OSSE 1 (blue), 3 (red), 10 (green) $fgCO_2$ of 4 FFNN
 621 outputs and NEMO/PISCES $fgCO_2$; shadow is the maximum and minimum values of differences from 4 FFNN $fgCO_2$
 622 for each OSSE. (a), (b) - estimates are available for all biomes presented in Figure 2 except biome 8; (c), (d) - biome 11;
 623 (e), (f) - biome 13; (g), (h) - biome 17.



624
 625 **Figure 9: Averaged number of Argo profiles per 5-day time step over 2008-2010 versus averaged differences between**
 626 **each OSSE $fgCO_2$ and NEMO $fgCO_2$ (in Pg/yr). (a) - all biomes; (b) - biome 11; (c) - biome 13; (d) - biome 17.**

627
 628
 629

Table 1: Information on Observation System Simulation Experiments.

Data	OSSE number	Period for training	averaged number of Argo floats per 5 days
SOCAT	OSSE 1	2001-2010	0
Argo (3°x3°)	OSSE 2	2008-2010	404
SOCAT + Argo (3°x3°)	OSSE 3	2001-2010 (SOCAT) + 2008-2010 (Argo)	403
SOCAT + Argo 25% (3°x3°)	OSSE 4	2001-2010 (SOCAT) + 2008-2010 (Argo)	101
SOCAT + Argo 10% (3°x3°)	OSSE 5	2001-2010 (SOCAT) + 2008-2010 (Argo)	40
SOCAT + Argo South (3°x3°)	OSSE 6	2001-2010 (SOCAT) + 2008-2010 (Argo South)	195



SOCAT + Argo 25% South (3°x3°)	OSSE 7	2001-2010 (SOCAT) + 2008-2010 (Argo South)	48
SOCAT + Argo 10% South (3°x3°)	OSSE 8	2001-2010 (SOCAT) + 2008-2010 (Argo South)	19
SOCAT + Argo S + Moorings	OSSE 9	2001-2010 (SOCAT) + 2008-2010 (Argo South, Moorings)	195
SOCAT + Argo S 25% + Moorings	OSSE 10	2001-2010 (SOCAT) + 2008-2010 (Argo South, Moorings)	48
SOCAT + Argo S 10% + Moorings	OSSE 11	2001-2010 (SOCAT) + 2008-2010 (Argo South, Moorings)	19

630
631

Table 2: Biomes from Fay and McKinley (2014) used for time series comparison (Fig. 2).

Number	Name
8	(Omitted) North Atlantic ice
9	Subpolar seasonally stratified North Atlantic
10	Subtropical seasonally stratified North Atlantic
11	Subtropical permanently stratified North Atlantic
12	Equatorial Atlantic
13	Subtropical permanently stratified South Atlantic
15	Subtropical seasonally stratified Southern Ocean
16	Subpolar seasonally stratified Southern Ocean
17	Southern Ocean ice

632
633
634

Table 3: Correlation coefficient and Standard Deviation (μatm) of 11 OSSEs from Table 2 estimated over 8 Atlantic Ocean biomes and at basin scale; the results are presented in Fig. 3.

Biome	All biomes	9	10	11	12	13	15	16	17
OSSE									
NEMO STD	25.34	28.17	17.29	19.59	17.89	18.84	15.20	10.79	24.03
OSSE 1	0.67/ 26.08	0.88/ 27.44	0.92/ 16.67	0.89/ 18.42	0.46/ 12.48	0.68/ 16.11	0.31/ 15.28	0.70/ 11.76	0.57/ 21.11
OSSE 2	0.89/ 22.82	0.91/ 22.28	0.96/ 17.09	0.97/ 19.14	0.83/ 15.42	0.92/ 18.19	0.76/ 8.89	0.87/ 9.43	0.90/ 19.56
OSSE 3	0.87/ 23.79	0.93/ 25.78	0.96/ 17.00	0.95/ 19.03	0.79/ 14.33	0.91/ 17.91	0.73/ 11.21	0.83/ 10.55	0.85/ 21.06



OSSE4	0.82/ 23.99	0.92/ 25.91	0.95/ 17.11	0.93/ 18.31	0.70/ 12.13	0.88/ 17.62	0.63/ 11.62	0.80/ 10.99	0.77/ 21.2
OSSE 5	0.80/ 24.18	0.92/ 26.48	0.94/ 17.16	0.92/ 18.83	0.65/ 11.39	0.86/ 16.95	0.59/ 11.86	0.75/ 11.3	0.75/ 20.58
OSSE 6	0.85/ 24.72	0.89/ 27.40	0.93/ 16.66	0.91/ 18.73	0.64/ 12.34	0.91/ 17.51	0.72/ 11.56	0.82/ 10.84	0.86/ 22.41
OSSE 7	0.82/ 24.48	0.89/ 27.87	0.93/ 16.32	0.91/ 18.19	0.54/ 11.17	0.88/ 17.33	0.66/ 11.71	0.80/ 11.12	0.80/ 20.90
OSSE 8	0.77/ 25.10	0.89/ 27.90	0.93/ 16.19	0.91/ 18.3	0.52/ 11.66	0.86/ 16.92	0.57/ 11.74	0.79/ 11.17	0.66/ 22.63
OSSE 9	0.88/ 24.51	0.92/ 28.17	0.95/ 16.11	0.94/ 17.67	0.68/ 12.98	0.92/ 17.84	0.72/ 11.31	0.84/ 10.89	0.91/ 21.63
OSSE 10	0.85/ 24.89	0.91/ 28.28	0.94/ 17.10	0.94/ 18.41	0.63/ 12.90	0.88/ 17.36	0.65/ 11.35	0.78/ 11.01	0.89/ 22.25
OSSE 11	0.83/ 24.67	0.91/ 28.39	0.93/ 16.4	0.93/ 18.10	0.58/ 13.20	0.86/ 16.79	0.56/ 11.29	0.74/ 10.96	0.88/ 21.92

635
 636
 637

Table 4: Normalised RMS differences and Biases (μatm) of 11 OSSEs from Table 2 estimated over 8 Atlantic Ocean biomes and at basin scale; the results are presented in Fig. 4.

Biome OSSE	All biomes	9	10	11	12	13	15	16	17
OSSE 1	14.13/ -4.25	11.63/ -3.26	6.32/ -0.39	6.63/ -2.93	15.41/ 0.17	12.5/ 2.12	15.97/ 1.32	8.08/ -5.41	17.33/ -11.63
OSSE 2	10.11/ 0.36	17.10/ -2.02	4.21/ 0.09	3.94/ 0.19	7.26/ 0.22	4.98/ 0.38	12.63/ -0.43	4.31/ -0.21	10.00/ 2.50
OSSE 3	8.32/ -0.46	9.59/ -0.32	4.56/ -0.30	4.24/ -0.71	8.00/ -0.14	5.73/ 0.57	11.87/ -0.85	4.20/ -0.97	10.18/ -0.66
OSSE 4	9.40/ -0.84	10.08/ -0.53	5.08/ -0.05	5.01/ -0.88	10.41/ -0.29	6.96/ 0.85	12.59/ -0.40	4.87/ -0.93	11.75/ -2.25
OSSE 5	9.82/ -1.46	10.43/ -0.83	5.50/ 0.50	5.35/ -0.98	11.11/ -0.25	7.93/ 0.85	12.72/ -0.54	5.71/ -1.69	11.80/ -4.02
OSSE 6	9.12/ -0.54	11.40/ -2.57	5.93/ 0.02	6.48/ -1.86	11.46/ 3.82	5.75/ 0.53	12.06/ -0.51	4.35/ -0.56	10.01/ -0.18
OSSE 7	9.75/ -1.22	11.79/ -2.64	6.16/ -0.10	6.26/ -2.68	13.30/ 3.77	6.90/ 0.58	11.97/ -0.56	4.90/ -1.68	11.03/ -1.80
OSSE 8	11.36/ -1.89	11.62/ -2.59	6.02/ 0.49	5.91/ -2.80	13.87/ 2.70	7.84/ 0.90	12.55/ -0.89	5.42/ -2.03	15.16/ -4.12
OSSE 9	8.37/ -0.44	10.58/ -2.52	5.47/ -0.001	5.13/ -1.33	11.34/ 2.91	5.37/ 0.41	12.18/ -0.88	4.16/ -0.75	8.51/ 0.37
OSSE 10	8.71/ -0.44	10.79/ -2.52	5.54/ -0.001	4.94/ -1.33	12.64/ 2.91	6.82/ 0.41	12.25/ -0.88	4.89/ -0.75	8.61/ 0.37



	-0.39	-2.35	0.79	-0.71	3.35	1.01	-0.92	-0.90	-0.21
OSSE 11	9.16/ -1.18	10.85/ -3.21	5.91/ -0.68	5.32/ -1.97	14.28/ 2.41	7.59/ 0.002	12.49/ -1.18	5.13/ -1.56	9.23/ -0.77

638

639 **Table 5: Differences (Eq. 4) between OSSE FFNN outputs and NEMO/PISCES $p\text{CO}_2$ and its standard deviation (STD)**
 640 **(Eq. 5) in μatm .**

Biome	Region 70°W- 30°E 80°S- 80°N	All 8 biomes	9	10	11	12	13	15	16	17
OSSE										
OSSE 1	-6.57/ 14.49	-6.57/ 13.54	-4.84/ 10.17	-1.46/ 6.98	-4.21/ 7.62	-2.03/ 13.88	0.11/ 13.88	-1.35/ 14.96	-8.04/ 8.99	-14.90/ 20.83
OSSE 3	-1.70/ 8.12	-1.50/ 7.15	-1.36/ 7.52	-0.90/ 4.62	-1.48/ 4.64	-1.49/ 7.09	-0.32/ 5.58	-1.93/ 7.16	-1.89/ 4.42	-2.05/ 10.59
OSSE 10	-2.34/ 8.64	-1.54/ 7.50	-3.54/ 8.59	-0.10/ 6.18	-1.52/ 5.42	1.93/ 9.38	-0.04/ 6.51	-2.15/ 8.18	-1.91/ 5.21	-1.55/ 8.99

641

642 **Table 6: Correlation coefficient between OSSEs and NEMO/PISCES $p\text{CO}_2$.**

Biome	Region 70°W- 30°E 80°S- 80°N	All 8 biomes	9	10	11	12	13	15	16	17
OSSE										
OSSE 1	0.68	0.67	0.88	0.92	0.89	0.46	0.68	0.31	0.70	0.57
OSSE 3	0.86	0.87	0.93	0.96	0.95	0.79	0.91	0.73	0.83	0.85
OSSE 10	0.85	0.85	0.92	0.94	0.94	0.63	0.88	0.65	0.78	0.89

643

644 **Table 7: $p\text{CO}_2$ averaged over the region 70°W-30°E 80°S-80°N and biomes from Fig. 2 for the NEMO/PISCES model**
 645 **and OSSEs 1, 3 and 10, as well as the corresponding averaged differences between OSSEs and NEMO/PISCES (in**
 646 **μatm).**

Biome	Region 70°W- 30°E 80°S- 80°N	All 8 biomes	9	10	11	12	13	15	16	17
OSSE										
NEMO	371.13	372.65	350.36	373.18	390.11	397.18	389.54	376.14	376.99	363.08
OSSE 1	367.09/ -4.04	368.39/ -4.25	347.10/ -3.26	372.78/ -0.39	387.17/ -2.93	397.36/ 0.17	391.66/ 2.12	377.46/ 1.32	371.58/ -5.41	351.44/ -11.63
OSSE 3	370.62/ -0.51	372.18/ -0.46	350.04/ -0.32	372.88/ -0.30	389.39/ -0.71	397.04/ -0.14	390.10/ 0.57	375.29/ -0.85	376.02/ -0.97	362.42/ -0.66



OSSE 10	370.14/ -0.99	372.26/ -0.39	348.01/ -2.35	373.98/ 0.79	389.39/ -0.71	400.53/ 3.35	390.55/ 1.01	375.22/ -0.92	376.09/ -0.90	362.87/ -0.21
---------	------------------	------------------	------------------	-----------------	------------------	-----------------	-----------------	------------------	------------------	------------------

647
 648
 649
 650

Table 8: $fgCO_2$ averaged over the region 70°W-30°E 80°S-80°N and biomes from Fig. 2 for the NEMO/PISCES model and OSSEs 1, 3, 4 and 10, as well as the corresponding averaged differences between each OSSEs and NEMO/PISCES (in Pg/yr).

Biome	Region 70°W-30°E 80°S-80°N	All 8 biomes	9	10	11	12	13	15	16	17
NEMO	-0.76	-0.70	-2.34	-1.14	-0.03	0.53	-0.004	-0.74	-0.50	-0.52
OSSE 1	-1.03/ -0.26	-0.99/ -0.28	-2.57/ -0.23	-1.17/ -0.03	-0.18/ -0.15	0.42/ -0.10	0.19/ 0.20	-0.68/ 0.06	-1.15/ -0.64	-1.17/ -0.65
OSSE 3	-0.80/ -0.04	-0.74/ -0.04	-2.36/ -0.02	-1.16/ -0.02	-0.07/ -0.03	0.49/ -0.04	0.05/ 0.06	-0.82/ -0.07	-0.61/ -0.10	-0.59/ -0.06
OSSE 10	-0.83/ -0.06	-0.74/ -0.04	-2.50/ -0.15	-1.09/ 0.04	-0.06/ -0.03	0.56/ 0.03	0.08/ 0.08	-0.82/ -0.07	-0.60/ -0.09	-0.56/ -0.03

651